ELECTRIC FIELD GRADIENTS IN MICRO/NANOFLUIDIC DEVICES

Shokufeh Kazemlou
Department of Chemical and Materials
Engineering, University of Alberta
Edmonton, Alberta, Canada

Neda Nazemifard
Department of Chemical and Materials
Engineering, University of Alberta
Edmonton, Alberta, Canada

ABSTRACT

Electrokinetic is one of the most important tools used to control the transport phenomena in micro/nanofluidic devices. To design a successful process, it is important to have a precise knowledge of parameters affecting electrokinetic transport. One of these parameters is the applied electric field. When the local values of the electric field deviate significantly from the nominal values, the assumption of a homogeneous field is an oversimplification resulting in failed or low efficiency processes. In this manuscript, the sources of inducing field gradients and their implications were investigated. Of particular interests are microfabricated arrays used extensively in microfluidic devices either as sieving matrices or mixing enhancers. A comprehensive parametric study was conducted to understand how the posts arrangements (hexagonal or square), distance and size, and surface charge change the field gradients. Our results provide criteria at which the assumption of uniform field is valid, which can have important implications in designing microfluidic units where either a high field gradient is favored (mixing) or not (separation).

INTRODUCTION

Microfluidics has been a rapid growing field during the last decade. Resent developments in micro-fabrication and micro-instrumentation have enabled fabrication of micro-devices with high functionality and complexity that can carry out most of chemical and biochemical processes. Miniaturization of these processes which led to the creation of the lab-on-a-chip systems necessitates developing new methods of manipulating transport in micro scale environments. Since most of liquid-solid interfaces bear an electrostatic charge, the application of an externally applied electric field results in the motion of the interface, a phenomena called electrokinetic. Electrokinetic is one of the most frequently used methods to control the transport phenomena in microfluidics. Basic electrokinetic phenomena such as electroosmosis or electrophoresis, where the applied electric field acts as the driving force, were employed in a variety of applications such as gel electrophoresis (Guttman, Cooke 1991, Fang, Zhang et al. 1996), chromatography (De Pra, Kok et al. 2008, Moore, Jaconson et al. 1995), capillary gel electrophoresis (Effenhauser, Paulus et al. 1994, Woolley, Mathies 1994), pulsed-field electrophoresis (Duke, Austin et al. 1996), insulated-based dielectrophoresis (Bhattacharya, Chao et al. 2011), electrodeless dielectrophoresis (Chou, Tegenfeldt et al. 2002). The adaptation of these techniques on microfluidic platforms have opened the possibilities of having lab-on-a-chip devices which ultimately can be used toward realization of personal medicine. To design a successful electrokinetic process, it is important to have a precise knowledge of parameters affecting electrokinetic transport. One of these parameters is the applied electric field. Effect of electric field and field gradients as important operational variables on electrophoresis and dielectrophoresis in microfabricated devices have been discussed in literature (Dorfman 2010, Chen, Fachin et al. 2011, Oh, Cheong et al. 2010). For some of processes, the nominal value of the field is sufficient to yield a correct calculation of the electrokinetic transport. However, when the local values of the field deviate significantly from the nominal values, the assumption of a homogeneous field is an oversimplification resulting in failed or low efficiency processes. For instance, during electrophoresis separation of DNA, the presence of field inhomogeneities can significantly compromise the separation resolution by increasing band broadening. Large gradients of the field can also affect the mobility or trajectory of molecules by introducing dielectrophoresis. The focus of this manuscript is to study the potential sources of inducing field gradients and their implications. Using finite element methods, the effect of microchip geometry, dielectric properties of the medium, and channels surface charge on the field magnitude and orientation have been evaluated. Of particular interests are microfabricated

arrays used extensively in microfluidic devices either as sieving matrices or mixing enhancers. A comprehensive parametric study is conducted to understand how the posts arrangements, distance and size, and surface charge change the field gradients.

METHOD

Mathematical Model

Electrokinetic processes can be described by the governing laws of electric fields, flow, species transport, heat transfer and chemical reactions. Many comprehensive works have been done on solving the flow and electric field equations for flow in microdevices (Bianchi, Ferrigno et al. 2000, Patankar, Hu 1998, MacInnes 2002). And more complete discussion of the electrokinetic equations can be found in the texts by Probstein (Probstein 1994), Hunter (Hunter 2001) and Deen (Deen 1998).

Several studies have investigated various microfluidic chips consisting of transverse microchannels (Kang, Joo et al. 2012, Cheng, Wang et al. 2012, Khandurina, Jacobson et al. 1999, Kuo, Shiu et al. 2007) and porous structures (Shiu, Whang et al. 2008, Kang, Li et al. 2010, Xu, Vaidya et al. 2003, Hanke, Waide et al. 2012) for different purposes of sample pretreatment, separation and detection of cells, particles and biomolecules.The geometry studied in this work (shown in Figure 1) is a common microfluidic chip design that has been used in several experiments such as analysis and fractionation of DNA molecules by Huang et al. (Huang, Tegenfeldt et al. 2002), Zeng et al. (Zeng, He et al. 2008), and Chou et al (Chou, Tegenfeldt et al. 2002). As shown in Figure 1, the microchipconsistsof a square chamber with a packed array of micron-scale posts, an injection channel, and several microchannelswhich surround the chamber and connect it to the electrodes, where voltages are applied.
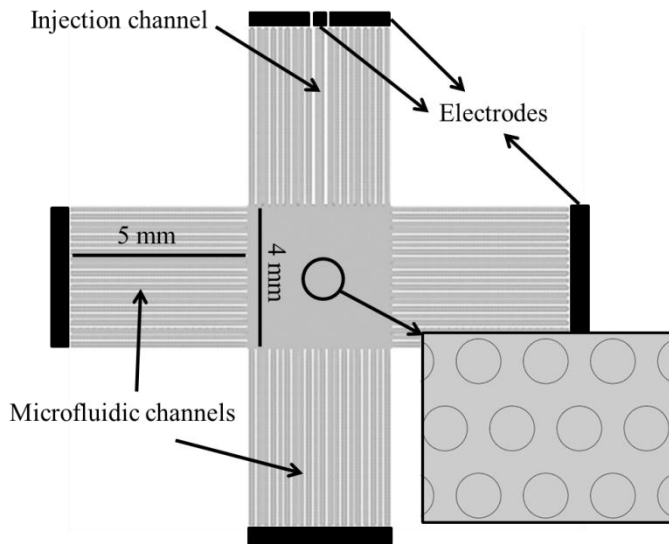

Figure 1. Schematic of the microfluidic chip studied in this work.The middle chamber consists ofmicro-fabricated arrays of posts. The injection channel and all the side microchannels are connected to the reservoirs where electrodes were used to apply electric voltages.

Our aim here is to calculate the electric field generated inside the microchip by applying the certain voltages at the channel reservoirs. We start our analysis with the conservation law for the chemical species in a fluid medium which is given by (Masliyah, Bhattacharjee 2006)

$$\frac{\partial c_i}{\partial t} = -\nabla . j_i + R_i \tag{1}$$

Where c_i is the concentration of the ith species, j_i is the ith species flux and R_i is the rate of production due to chemical reaction per unit volume. j_i has the contributions from convection, diffusion and migration under the influence of external forces. The external force here is the electrical force $F_{EL} = q_i \, E = - q_i \nabla \psi$, produced through applying voltages on the channels.Therefore j_i can be obtained from the Nernst – Planck equation (Masliyah, Bhattacharjee 2006)

$$j_i = c_i u - D_i - \mu_i c_i \nabla \psi \tag{2}$$

Where D_i is the diffusivity of the ith species, μ_i is mobility of the ith species and ψ is the electrical potential. In the steady state condition and the absence of chemical reaction, equation 1 will be reduced to

$$\nabla . j_i = 0 \tag{3}$$

The current density, which is the result of the individual flux of all the ionic species present in the electrolyte solution, is given by (Masliyah, Bhattacharjee 2006)

$$i = F \sum z_i \, j_i \tag{4}$$

Where F is the Faraday constant and z_i is the valence of the ith species. In term of ionic molar concentration, Eq. 2, it can be written as

$$i = Fu \sum z_i \, c_i - F \sum D_i z_i \nabla c_i - \frac{F^2}{RT} \nabla \psi \sum z_i^2 \, D_i c_i \tag{5}$$

In an electrically neutral electrolyte solution,$\sum z_i \, c_i = 0$, with no concentration gradient, $\nabla c_i = 0$, equation 5 is reduced to

$$i = -\sigma \nabla \psi \tag{6}$$

Where

$$\sigma = \frac{F^2}{RT} [\sum z_i^2 \, D_i c_i] \tag{7}$$

And σ is the electric conductivity of the solution. Taking the divergence of the Eq. 4 gives

$$\nabla \cdot i = F \sum z_i (\nabla \cdot j_i) \qquad (8)$$

Considering the Eq. 3 one can write

$$\nabla \cdot i = 0 \qquad (9)$$

Substituting the Eq. 6 into Eq. 9 yields the Laplace equation for the potential

$$\nabla^2 \psi = 0 \qquad (10)$$

Throughout the analysis above, the assumption of constant mobility, diffusivity and conductivity has been made.

Table 1. Values of physicochemical properties of the modeled system employed in the simulations

property	value
thickness of the microdevice, d	10 μm
space charge density, ρ	0 C/m^3
permittivity of vacuum, ε_0	8.85×10^{-12} C/Vm
relative permittivity of the buffer solution, ε_1	70
relative permittivity of the posts, ε_2	1.5

Numerical Simulation

Finite element method was used to calculate electric field by solving Eq. 2 in the two dimensional geometry as shown in Figure 1. Commercially available software, COMSOL 3.5a, is used to carry out the numerical simulation. Using COMSOL's multiphysics capabilities, two series of simulations were performed in this work. The electrostatic mode was used which solves the following equation:

$$- \nabla \cdot d\varepsilon_0 \varepsilon_r \nabla V = d\rho \qquad (8)$$

Where d is the thickness of the device, ε_0 is the vacuum permittivity, ε_r is the relative permittivity and ρ is the space charge density. The values of these parameters employed in our simulations are listed in Table 1. Since d, ε_0, ε_r and ρ are constant values, the Eq. 8 is simplified to:

$$- \nabla^2 V = 0 \qquad (9)$$

So as it was expected, the model solves the Laplace equation for the potential field. The electric field is obtained by solving the equation $E = - \nabla V$. Figure 2 illustrates the geometry of the 2D microfluidic chip studied in our simulations. It consists of a 4×4 mm^2 square chamber connected to 20 microchannels (100 μm $\times$ 5 mm, 100 μm periodically) on three sides and 18

microchannels and an injection channel (200 μm $\times$ 5 mm) on the fourth side. The default boundary conditions are zero charge everywhere except on the reservoirs where specific voltages were applied. All the reservoirs on the top and left-hand side of the chamber carry the same potential of -V, the reservoirs on the bottom and right-hand side of the chamber have the same potential of V, and the injection channel receives a smaller potential υ. Table 2 presents the ranges of V and υ employed in the simulations. Two series of simulations were conducted; i) electric field orientation inside the microchip was calculated to define a domain inside the chamber where the field orientations are the same as nominal values. In this part, the chamber did not contain the post arrays, ii) electric field gradients were calculated in the chamber with post arrays. The array consists of a regular lattice of posts of diameter d and surface-to-surface spacing a. The ranges of d and a employed in our simulations are presented in Table 2.
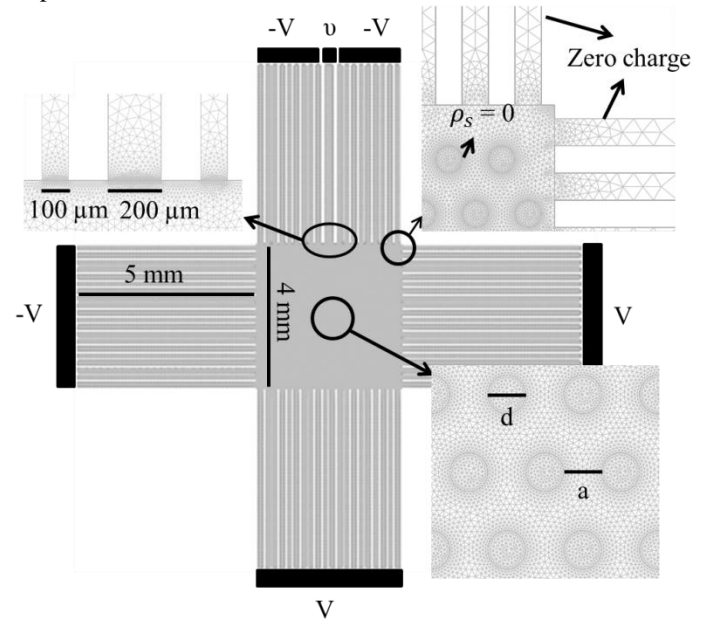

Figure 2. Schematic of the geometry solved in our simulations illustrating the dimensions and boundary conditions. The middle chamber consisting of post arrays is 4 mm $\times$ 4 mm, and the posts are of diameter d and surface-to-surface spacing a. The channels, which are 5 mm in length, were connected to electrodes where certain voltages were applied. Surface charge of the posts (ρ_s) is zero and zero charge condition is applied to the interior surface of the channels.

Two arrangements of the arrays i.e., hexagonal and square (Figs. 3A and B), and three post cross sections i.e., circular, rectangular, and rhombic (Figs. 3C, D, and E) were considered. A triangular mesh configuration was used to discretisize the geometry in order to solve the Laplace equation. Instead of a uniform mesh configuration, a more refined mesh configuration was used in the vicinity of the posts, sharp corners, and along the intersections where the to insure the accuracy of the calculation. Finite element analysis was applied in a triangular mesh of around 400 000 elements and 200 000 nodal points. It was observed that such a refined mesh configuration was

sufficient to provide electric field values which are independent of the number of elements.

RESULTS AND DISCUSSION

i) Electric field orientation
The 2D simulation with COMSOL Multiphysics provided a measure to define an area where the field orientation can be assumed constant and equal to its nominal value. In what

Table 2. The ranges of some parameters in the simulations

parameter	value
magnitude of the voltage applied on the microchannels, V	(70, 280) V
voltage applied on the injection channel, υ	(-160, -40) V
diameter of the posts, d	(25, 400) μm
spacing between the posts, a	(25, 400) μm
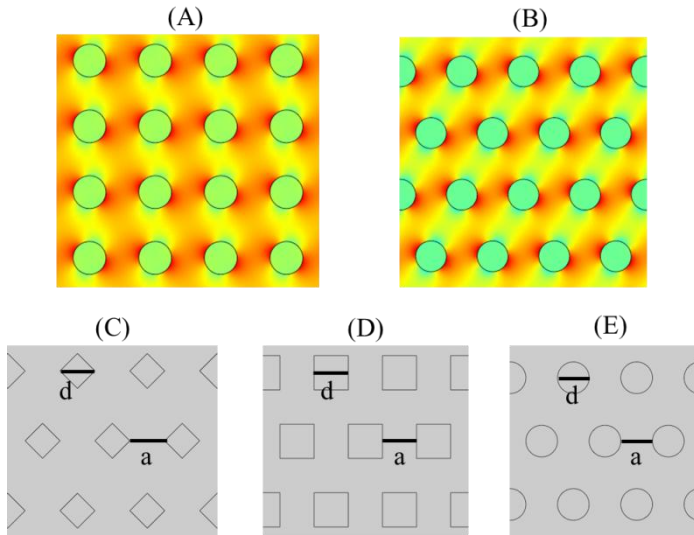
Figure 3. Schematic representation of (A) square and (B) hexagonal arrangements of microfabricated array with the posts of (C) rhombic type, (D) rectangular type and (E) circular type.

follows, this area will be called "safe zone". Figure 4A depicts the safe zone for a symmetric microchip. Comparing to the geometry shown in Figure 2, the injection channel is replaced by two microchannels in this geometry so all four sides of the chamber are exactly the same. It can be seen from the Figure 4 that the safe zone is a square in the middle of the microchip with equal spacing from the sides of the chamber. In order to investigate the effect of size, three microchips of different sizes (2mm, 4mm and 8mm chambers) were considered with the applied voltages being changed proportional to the size to maintain the same field strengths. It was observed that the safe zone is linearly proportional in size to the microchip size and

the sufficient spacing from the sides of the chamber is 14.5% of the chamber size for any sizes of the chamber. Figure 4B depicts the safe zone for the microchip shown in Figure 2 with the injection channel. The addition of the injection channel rendered the geometry to asymmetric and consequently shrank the dimensions of the safe zone. A comparison between Figures 4A and B shows that the spacing between the safe zone and the chamber wall has changed from 14.5 % to 23 % by the addition of the injection channel.
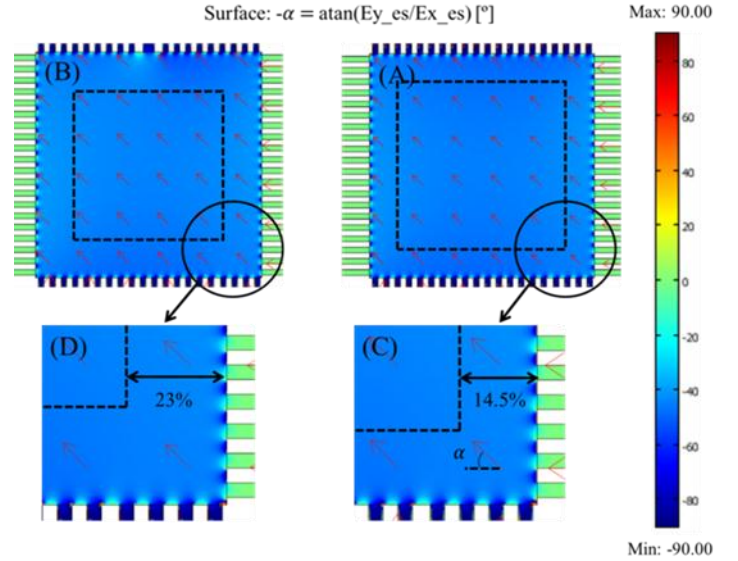

Figure 4. Schematic representation of the safe zone for (A) a symmetric geometry with no injection channel and (B) the asymmetric geometry shown in Figure 2. Spacing between the safe zone and the chamber walls is (C) 14.5% of the chamber size for the symmetric geometry and (D) 23% for the asymmetric geometry.
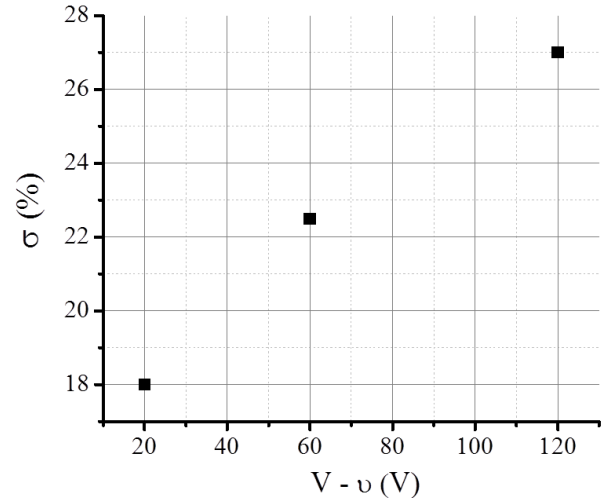

Figure 5. Spacing between the safe zone and the chamber walls, σ (shown as the percentage of the chamber size), versus voltage difference of the injection channel and microchannels (V – υ).

By changing the difference between the voltage applied at the injection channel (υ) and the voltage applied at the other channels (V), it was observed that the size of the safe zone decreased by increasing the voltage difference (V-υ) as shown in Figure 5.

The effect of surface charge of the interior surfaces of the chamber and the channels on the shape and size of the safe zone was also studied and the results are shown in Figure 6.

Figures 6A and 6B illustrate how the safe zone varies by different values of the surface charge. It can be seen that positive and negative charges have different influences on the safe zone.
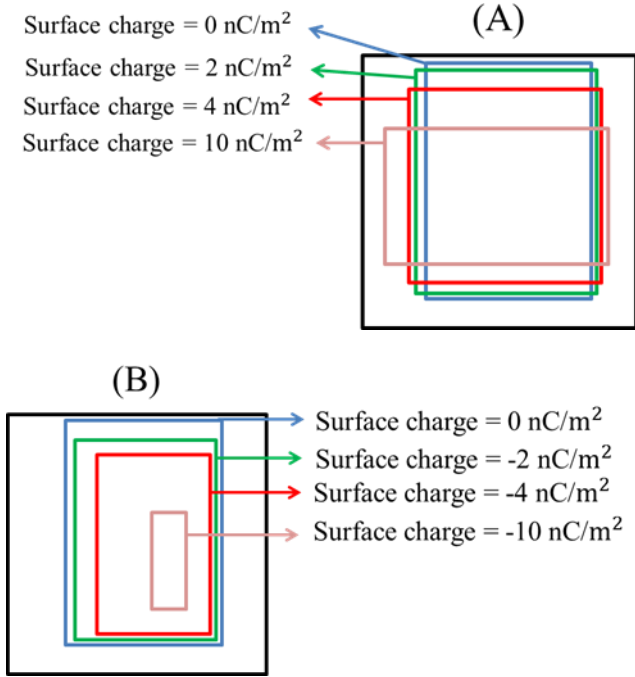
Figure 6. Schematic illustrates the effect of (A) positive surface charges and (B) negative surface charges on the shape and size of the safe zone.

ii) Electric field and field gradients

Electric field and filed gradients were calculated in a microchip shown in Figure 2 where the chamber consists of arrays of posts. A parametric study was conducted to investigate the effect of diameter, distance between the posts, shape of the posts and the post array arrangement on the electric filed and field gradients. Figure 7A shows the electric field calculated in a micro-fabricated array geometry with circular posts. In order to minimize the effects of the channel wall on the results, a unit cell in the middle of the chamber was considered where the field and field gradients were averaged over area of the unit cell as shown in Figure 7B. In what follows, the values of the field and field gradients employed to make the graphs are the averaged values over this area. Figure 8 presents the variation

of the field with respect to the distance between the posts, a, for three post cross sections i.e., circular, rectangular, and rhombic. It should be noted here that the value of the diameter was kept constant and equal to 100μm. It is evident from Figure 8 that the electric field decreases as the distance increases regardless of the post shape. It can be seen that for each value of a, the greatest value of the field belongs to the rectangular posts and the lowest value belongs to the rhombic posts.
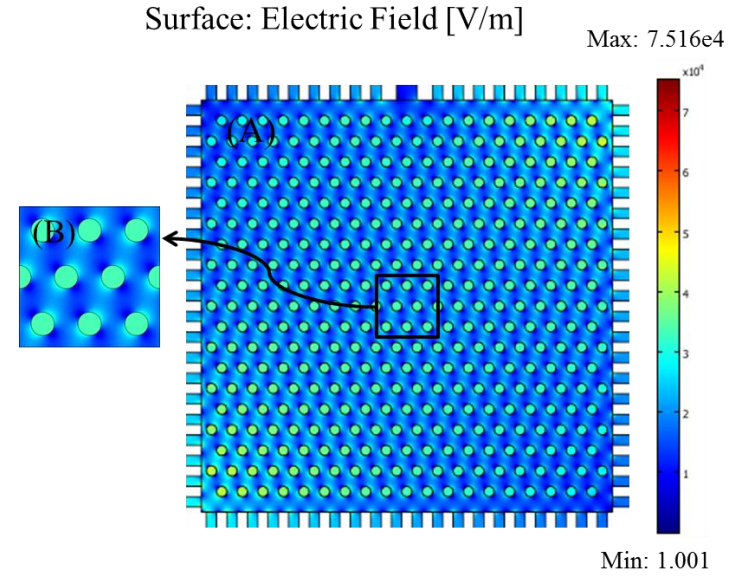

Figure 7. (A) Electric field calculated in a micro-fabricated array arrangement with circular posts. (B) Schematic presentation of the unit cell over which the average of the field and field gradients employed in our evaluations in this work were calculated.
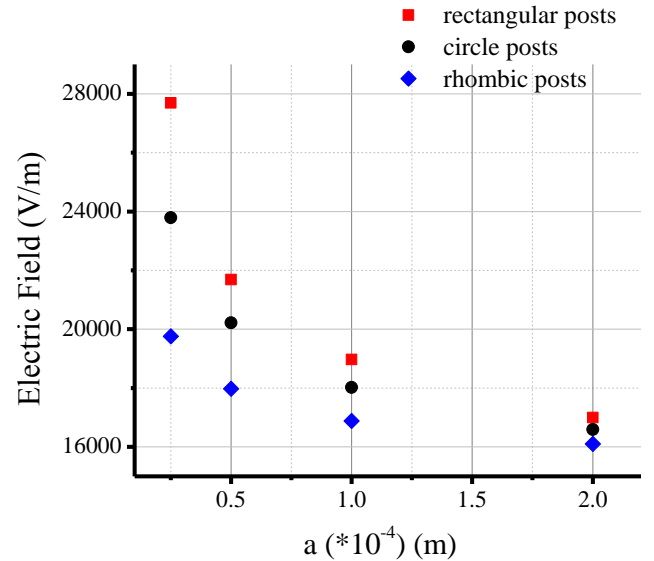

Figure 8. Variation of the electric field with respect to distance between the posts for the posts of different type: circular, rectangular and rhombic. The field decreases as the distance increases.

The variation of the field with respect to diameter of the posts was evaluated as well. Figure 9 plots the electric field versus diameter of the posts for all circular, rectangular and rhombic posts. Note that the post-to-post distance was kept constant and equal to 100μm. One can see from Figure 9 that the field increases by increasing the diameter of the posts. It can be seen from this figure that the effect of diameter on the value of the electric field for rectangular posts is more than circular and rhombic posts, i.e. by changing the diameter of the post the structure which has rectangular posts experiences the most variation in the value of the electric field in compare to the structures with circular or rhombic posts.
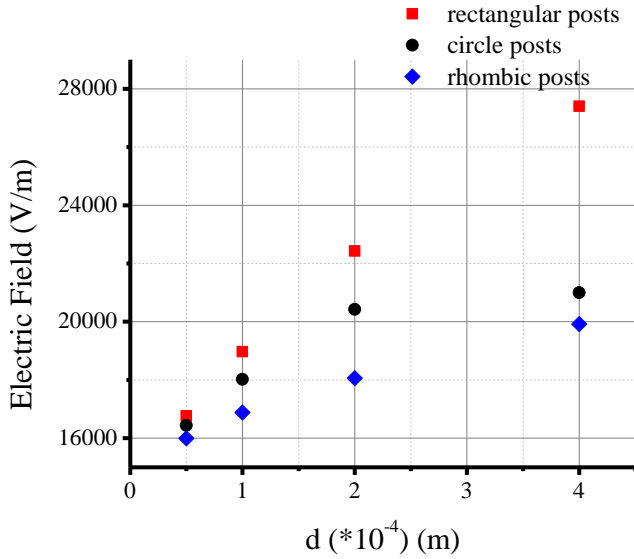

Figure 9. Relation between the field and diameter of the posts for circular, rectangular and rhombic posts. The field increases by increasing the diameter of the posts.

Figure 10 presents the distribution of the electric field over the unit cell area for three types of posts (circular, rectangular and rhombic). It can be obtained from this figure that the extremums of the electric field take place in the corners of the posts for rectangular posts (Fig. 10B). For circular posts the extremums take place in the direction of the electric field orientation (Fig. 10A).

In the structure with rhombic posts the field extremums are located in the corners of the posts and also in the direction of the field orientation (Fig. 10C). As one can see from Figure 10B the field orientation is in the direction of diagonal of the rectangular posts and it can be seen that for a specific structure with the same values of d and a, the geometry with rectangular posts experiences the highest maximum value of the electric field rather than the structures with circular or rhombic posts. Regarding the variation of the field with respect to diameter and distance between the posts (Figs. 8 and 9) we also evaluated the relation between the field and d/a ratio.
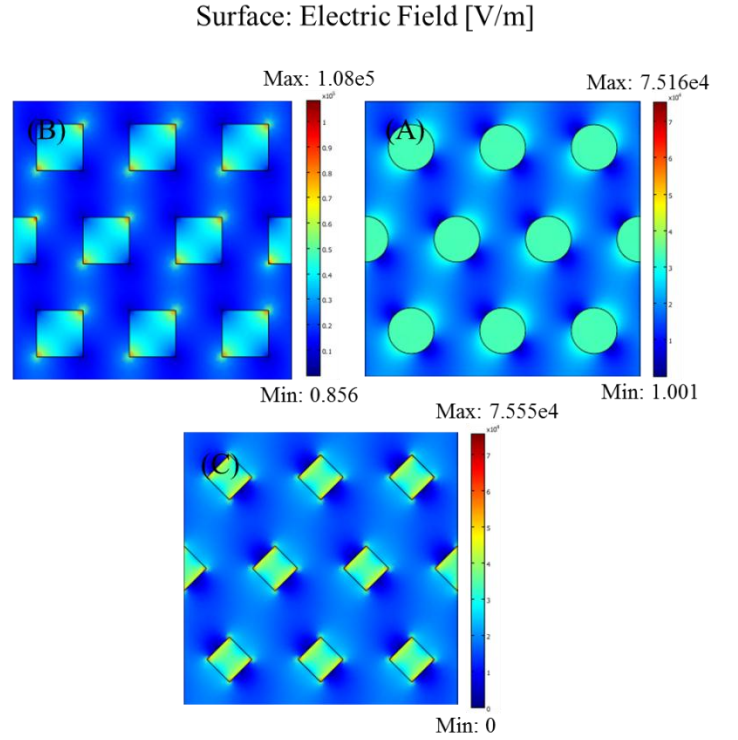
Surface: Electric Field [V/m]

Figure 10. Schematic illustrates the electric field distribution and position of the field local extremums in the structures with (A) circular posts (B) rectangular posts and (C) rhombic posts.

Figure 11 plots the field versus d/a ratio. It can be observed from this figure that the field monotonously increases by increasing d/a ratio.
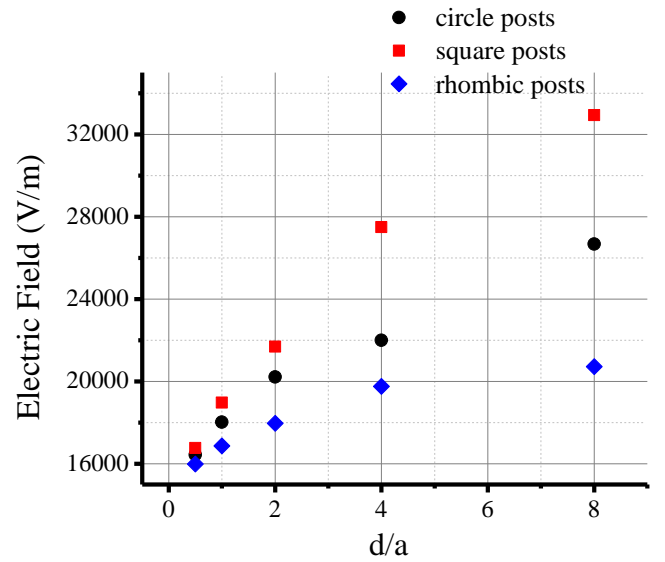

Figure 11. Relation between the field and d/a ratio for circular, rectangular and rhombic posts. The field monotonously increases as d/a ratio increases.

Since the d/a ratio is a combination of diameter and distance between the posts it can be used as a meaningful parameter in designing the micro-structures including post arrays.

Figure 12 plots the field gradients versus the distance between the posts, *a*. According to Figure 12, the field gradient decreases as the distance between the posts increases. Also this figure demonstrates that for all values of *a*, the highest field gradient is present for the geometry with rectangular post.
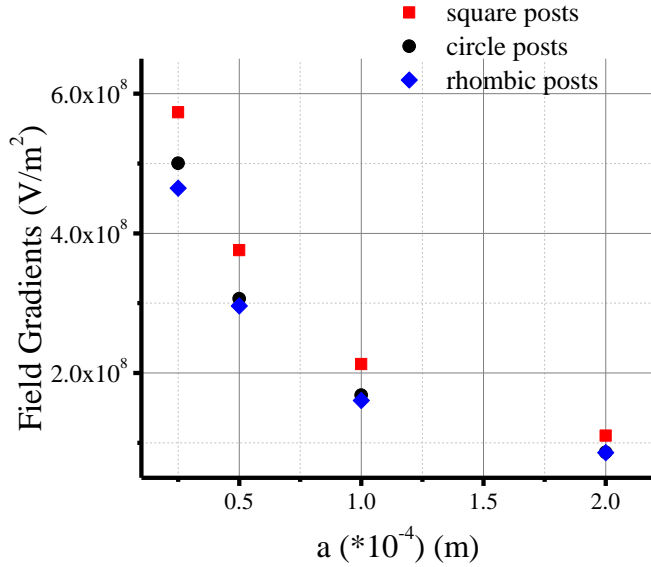

Figure 12. Variation of the field gradients with respect to distance between the posts for the posts of different type: circular, rectangular and rhombic. The field gradients decrease as the distance increases.
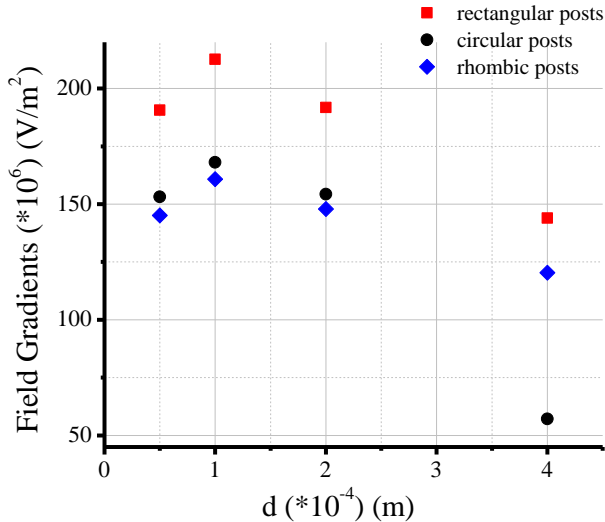

Figure 13. Relation between the field gradients and diameter of the posts. The variation of the field gradients with respect to diameter is not monotonous. Geometry with rectangular posts experiences the highest field gradients in compare to the geometries with circular or rhombic posts.

Figure 13 shows the variation of the field gradients with respect to diameter of the posts. It can be seen from this figure that the field gradients don't change monotonously by changing the diameter of the posts. It is evident from the figure that for all values of d, the highest field gradients belong to structure with rectangular posts.

Seeking for a parameter with which the field gradient varies monotonously, we came up with the parameter $N.d.a^{-1}$. N is total number of the posts in each structure. Figure 14 plots the variation of the field gradients with respect to $N.d.a^{-1}$. Formerly it was obtained that the field monotonously increases by increasing d/a ratio. Figure 14 demonstrates that the field gradients monotonously increase by increasing $N.d.a^{-1}$ which is the product of total number of the posts and d/a ratio. Therefore this parameter can be employed in designing the micro-structures with post arrays for the applications in which the field gradient is of importance.
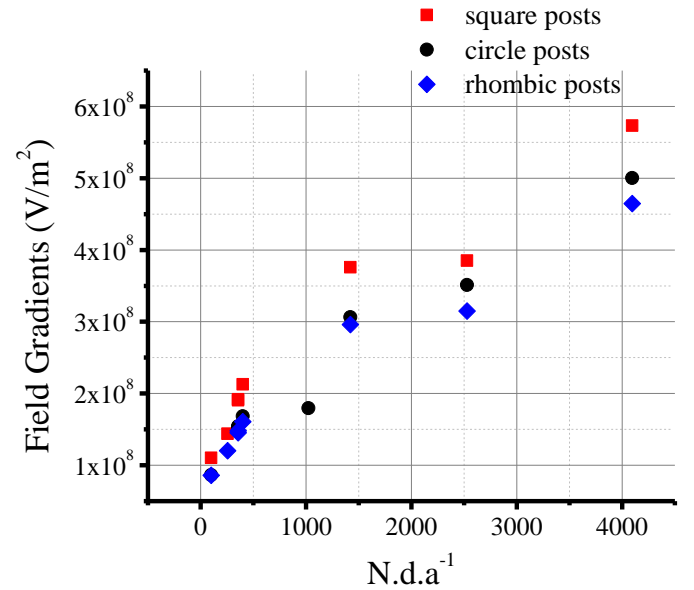

Figure 14. Variation of the field gradients with respect to the parameter $N.d.a^{-1}$ for circular, rectangular and rhombic posts.

Figure 15 illustrates distribution of the field gradients over the unit cell area for the structures with circular, rectangular and rhombic posts. The extremums of the field gradients take place in the corners of the rectangular and rhombic posts. It can be observed from this figure that the highest field gradients belong to geometry with rectangular posts and then to geometry with rhombic posts.
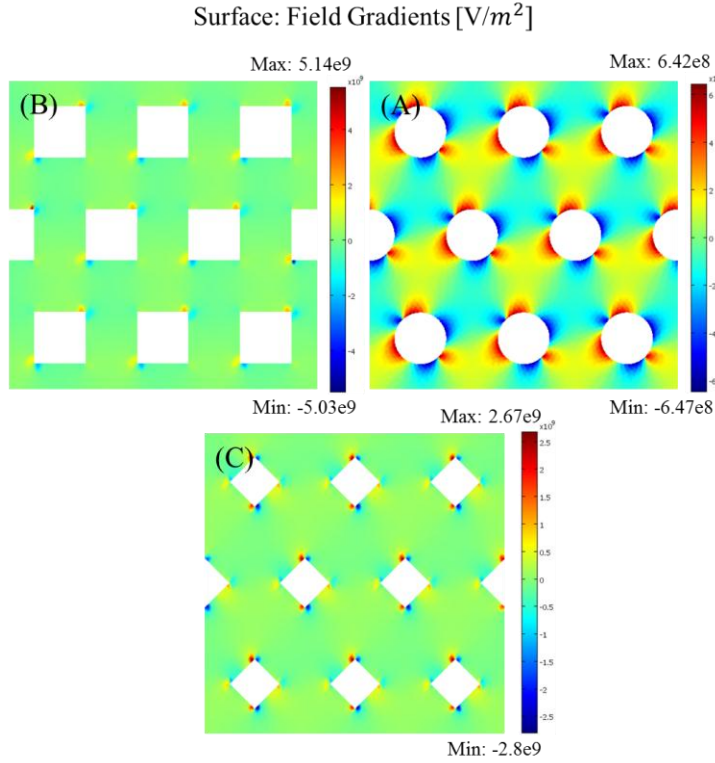
Surface: Field Gradients [V/m^2]

Figure 15. Schematic representation of the field gradients and their extremums over the unit cells of structures with (A) circular posts, (B) rectangular posts and (C) rhombic posts. The highest field gradient belongs to structure with rectangular posts.
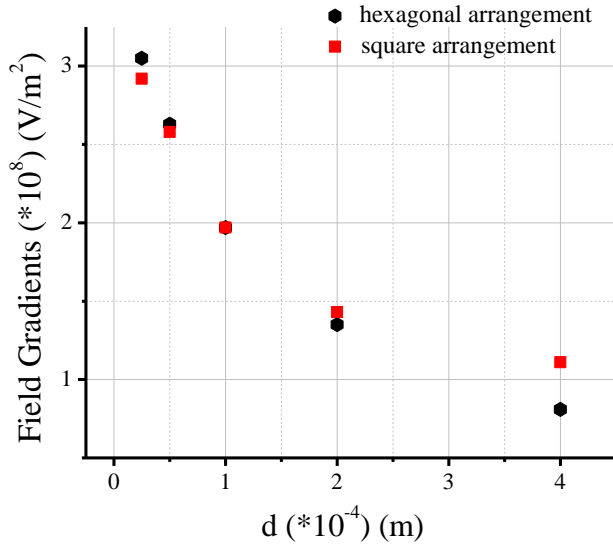

Figure 16. Variation of the field gradient with respect to diameter for the circular posts in two different arrangements: hexagonal and square.

To investigate the effect of post arrangement on the field gradients, structures with square arrangement were created and results are presented in Figure 16. From Figure 16 it can be seen that for *d<a*, the square arrangement provides larger values of the field gradients in compare to the hexagonal arrangement. On the other hand, for *d>a*, the hexagonal arrangement yields larger field gradients. For *d = a* both arrangements experience the equal values of the field gradients.

CONCLUSION

The electric field gradient and orientation in a micro-fabricated array structure was calculated numerically using finite element method. It was observed that in the vicinity of the junction between the chamber and microchannels, the field orientation significantly deviates from its nominal values. We defined a "safe zone" in the chamber where this deviation is less than 5%. Our calculations showed that the dimension of this zone is affected by the chamber size, channels surface charge, and the difference between the voltages applied in the injection channel and side channels. A symmetric microchip with zero surface charge on the wall had the largest safe zone meaning it can maintain the nominal values of the field orientation across the chamber.

Electric field and field gradient were also calculated in a micro-fabricated array geometry. It was observed that the electric field increased by increasing the diameter and decreasing the post-to-post distance. It was also obtained that the field monotonously increases by increasing d/a ratio. So this parameter can be helpful in designing the micro-fabricated structures with the arrays of posts which have applications where electric field value is of importance. In addition, it was seen that rectangular posts experienced highest value of electric field compared to the circular and rhombic posts.

The field gradients were observed to be decreased by increase in post-to-post distance and there was no relation obtained between field gradients and diameter of the posts. It was seen that the field gradients increase monotonously by parameter N.d.a^{-1}. This relation implies that in addition to d and a, the total number of the posts is also affecting the field gradients. N.d.a^{-1} can be used in designing micro-fabricated devices with post arrays for applications in which the field gradients values are important. It was observed that geometries with rectangular posts induce highest value of the field gradients compared to the geometries with circular or rhombic posts. It was also observed that the extremums of the field gradients take place in the corners of the posts.

The effect of array arrangement on the field gradient was observed to be dependent on the *d/a* ratio. For *d/a< 1*, the square arrangement provides larger values of the field gradients, whereas, for *d/a> 1*, the hexagonal arrangement yields larger field gradients. For *d/a = 1* both arrangements exhibits the equal values of the field gradients.

REFERENCES

[1] Bhattacharya, S., Chao, T., and Ros, A., 2011, "Insulator-Based Dielectrophoretic Single Particle and Single Cancer Cell Trapping," Electrophoresis, **32**(18) pp. 2550-2558.

[2] Bianchi, F., Ferrigno, A., and Girault, H., 2000, "Finite Element Simulation of an Electroosmotic-Driven Flow Division at a T-Junction of Microscale Dimensions," Analytical Chemistry, **72**(9) pp. 1987-1993.

[3] Chen, G. D., Fachin, F., Fernandez-Suarez, M., 2011, "Nanoporous Elements in Microfluidics for Multiscale Manipulation of Bioparticles," Small, **7**(8) pp. 1061-1067.

[4] Cheng, S., Wang, Z., Ge, S., 2012, "Rapid Separation of Four Probiotic Bacteria in Mixed Samples using Microchip Electrophoresis with Laser-Induced Fluorescence Detection," Microchimica Acta, **176**(3-4) pp. 295-301.

[5] Chou, C., Tegenfeldt, J., Bakajin, O., 2002, "Electrodeless Dielectrophoresis of Single- and Double-Stranded DNA," Biophysical Journal, **83**(4) pp. 2170-2179.

[6] De Pra, M., Kok, W. T., and Schoenmakers, P. J., 2008, "Topographic Structures and Chromatographic Supports in Microfluidic Separation Devices," Journal of Chromatography a, **1184**(1-2) pp. 560-572.

[7] Deen, W.M., 1998, "Analysis of transport phenomena," Oxford University Press, Oxford, .

[8] Dorfman, K. D., 2010, "DNA Electrophoresis in Microfabricated Devices," Reviews of Modern Physics, **82**(4) pp. 2903-2947.

[9] Duke, T., Austin, R., Cox, E., 1996, "Pulsed-Field Electrophoresis in Microlithographic Arrays," Electrophoresis, **17**(6) pp. 1075-1079.

[10] Effenhauser, C., Paulus, A., Manz, A., 1994, "High-Speed Separation of Antisense Oligonucleotides on a Micromachined Capillary Electrophoresis Device," Analytical Chemistry, **66**(18) pp. 2949-2953.

[11] Fang, Y., Zhang, J., Hou, J., 1996, "Activation Energy of the Separation of DNA Sequencing Fragments in Denaturing Noncross-Linked Polyacrylamide by Capillary Electrophoresis," Electrophoresis, **17**(9) pp. 1436-1442.

[12] Guttman, A., and Cooke, N., 1991, "Capillary Gel Affinity Electrophoresis of Dna Fragments," Analytical Chemistry, **63**(18) pp. 2038-2042.

[13] Hanke, C., Waide, S., Kettler, R., 2012, "Monitoring Induced Gene Expression of Single Cells in a Multilayer Microchip," Analytical and Bioanalytical Chemistry, **402**(8) pp. 2577-2585.

[14] Huang, L., Tegenfeldt, J., Kraeft, J., 2002, "A DNA Prism for High-Speed Continuous Fractionation of Large DNA Molecules," Nature Biotechnology, **20**(10) pp. 1048-1051.

[15] Hunter, R.J., 2001, "Foundations of colloid science," Oxford University Press, Oxford, .

[16] Kang, C. M., Joo, S., Bae, J. H., 2012, "In-Channel Electrochemical Detection in the Middle of Microchannel Under High Electric Field," Analytical Chemistry, **84**(2) pp. 901-907.

[17] Kang, Q., Li, Y., Xu, J., 2010, "Polymer Monolith-Integrated Multilayer Poly(Dimethylsiloxane) Microchip for Online Microextraction and Capillary Electrophoresis," Electrophoresis, **31**(18) pp. 3028-3034.

[18] Khandurina, J., Jacobson, S., Waters, L., 1999, "Microfabricated Porous Membrane Structure for Sample Concentration and Electrophoretic Analysis," Analytical Chemistry, **71**(9) pp. 1815-1819.

[19] Kuo, C., Shiu, J., Wei, K. H., 2007, "Monolithic Integration of Well-Ordered Nanoporous Structures in the Microfluidic Channels for Bioseparation," Journal of Chromatography a, **1162**(2) pp. 175-179.

[20] MacInnes, J., 2002, "Computation of Reacting Electrokinetic Flow in Microchannel Geometries," Chemical Engineering Science, **57**(21) pp. 4539-4558.

[21] Masliyah, J.H., and Bhattacharjee, S., 2006, "Electrokinetic and colloid transport phenomena," Wiley, .

[22] Moore, A., Jacobson, S., and Ramsey, J., 1995, "Microchip Separations of Neutral Species Via Micellar Electrokinetic Capillary Chromatography," Analytical Chemistry, **67**(22) pp. 4184-4189.

[23] Oh, D., Cheong, I. C., Lee, H. G., 2010, "Fast Microchip Electrophoresis using Field Strength Gradients for Single Nucleotide Polymorphism Identification of Cattle Breeds," Bulletin of the Korean Chemical Society, **31**(7) pp. 1902-1906.

[24] Patankar, N., and Hu, H., 1998, "Numerical Simulation of Electroosmotic Flow," Analytical Chemistry, **70**(9) pp. 1870-1881.

[25] Probstein, R.F., 1994, "Physicochemical hydrodynamics " Wiley, .

[26] Shiu, J., Whang, W., and Chen, P., 2008, "Behavior of Single DNA Molecules in the Well-Ordered Nanopores," Journal of Chromatography a, **1206**(1) pp. 72-76.

[27] Woolley, A., and Mathies, R., 1994, "Ultra-High-Speed Dna Fragment Separations using Microfabricated Capillary Array Electrophoresis Chips," Proceedings of the National Academy of Sciences of the United States of America, **91**(24) pp. 11348-11352.

[28] Xu, Y., Vaidya, B., Patel, A., 2003, "Solid-Phase Reversible Immobilization in Microfluidic Chips for the Purification of Dye-Labeled DNA Sequencing Fragments," Analytical Chemistry, **75**(13) pp. 2975-2984.

[29] Zeng, Y., He, M., and Harrison, D. J., 2008, "Microfluidic Self-Patterning of Large-Scale Crystalline Nanoarrays for High-Throughput Continuous DNA Fractionation," Angewandte Chemie-International Edition, **47**(34) pp. 6388-6391.